RSC Advances

PAPER

View Article Online
View Journal | View Issue



Cite this: *RSC Adv.*, 2018, **8**, 39879

# Designed formation of $Co_3O_4$@$NiCo_2O_4$ sheets-in-cage nanostructure as high-performance anode material for lithium-ion batteries†

Xuefeng Chu,* Chao Wang, Lu Zhou, Xingzhen Yan, Yaodan Chi and Xiaotian Yang*

Received 5th September 2018
Accepted 23rd November 2018

DOI: 10.1039/c8ra07396a

rsc.li/rsc-advances

Structural and compositional control of functional nanoparticles is considered to be an efficient way to obtain enhanced chemical and physical properties. A unique $Co_3O_4$@$NiCo_2O_4$ sheets-in-cage nanostructure is fabricated *via* a facile conversion reaction, involving subsequent hydrolysis and annealing treatment. Such hollow nanoparticles provide an excellent property for Li storage.



Recently, the development of low-cost and environment-friendly renewable energy conversion and storage systems has become a research focus to address the increasingly serious energy crisis and environment issues.[1–3] Lithium-ion batteries (LIBs), as one of the most important energy storage technologies, have received tremendous attention in the past decades.[4–8] Among the various anode materials, Co-based transition metal oxides have been widely investigated owing to their higher theoretical capacity compared with the traditional anode electrode, graphite (372 mA h $g^{-1}$).[9–13] However, such kind of anodes usually suffer from the large volume changes during the long-term charge/discharge process, as well as the low conductivity, which are the main reasons for the fast fading in capacity and poor rate performance.

One efficient way to solve the problem is the construction of complex hollow nanostructures instead of traditional solid ones.[14–17] The complex hollow nanostructures have some unique advantages, such as the larger specific surface area, well-defined inner hollow space and increased surface permeability. These factors are favourable for the fast mass/charge transfer, resulting in highly increased property for lithium storage. To date, many kinds of synthetic strategies have been successfully developed and reported. As examples, Wang and co-workers reported a facile synthesis of multi-shelled $Co_3O_4$ nanospheres with controllable shells.[18] Carbon nanospheres are pre-synthesized and used as the hard templates to adsorb the $Co^{2+}$ ions, followed by an annealing treatment in air for the final conversion of $Co_3O_4$ crystals. Lou's group synthesized a series of Co-based complex hollow nanostructures.[19–22] $Co_3O_4$@$NiCo_2O_4$,[19] $Co_3O_4$@Co–Fe mixed oxide[20] and $Co_3O_4$@$Co_3V_2O_8$ triple-shelled nanocages[21] are successfully fabricated. Otherwise, $Co_3O_4$ bubbles/N doped carbon,[23] $Co_3O_4$ hollow nanospheres with ultra-thin nanosheets as building blocks,[24] and $Co_3O_4$/N doped carbon nanocubes[25] are also prepared. Benefiting from the unique structural features, these hollow materials always show highly enhanced electro-chemical properties. In addition, using heteroatoms to couple with Co metal to form the mixed metal compound is considered as another effective way to increase the LIB performance. Such mixed metal compounds are favourable for controlling the local chemical environment and modulating the synergistic effect between etch component. More importantly, the coupling of different kinds of metal ions together can bring richer redox reactions and higher electronic conductivity, resulting in significant enhancement of the LIB performance.[26–31] $NiCo_2O_4$ hollow spheres,[27,28] hollow polyhedrons,[29] nanoarrays,[30] and $ZnCo_2O_4$/carbon cloth hybrids[31] are fabricated and used as high-performance anodes for LIBs. Therefore, a rational design and synthesis of Co-based functional nanomaterials with complex inner hollow nanostructure and multi-component-coupled outer surface is expected to yield the increased LIB performance.

In the past two decades, metal–organic frameworks (MOFs) have been widely used as sacrificial templates for the synthesis of functional materials.[19–21,32–39] The MOFs have some distinctive structural and compositional advantages, such as high porosity and easily controllable composition. Furthermore, the chemical and thermal instability makes the conversion reaction occur easily, that MOFs can transform to functional nanoparticles *via* a facile ion-exchange reaction or annealing treatment in a specific atmosphere. Among the variety of MOFs, Co-based zeolitic imidazolate framework-67 (ZIF-67) has received continues attention and been widely studied. As successful examples, 2-methylimidazole ligand in ZIF-67 can be easily

*Jilin Provincial Key Laboratory of Architectural Electricity & Comprehensive Energy Saving, School of Electrical and Electronic Information Engineering, Jilin Jianzhu University, Changchun 130118, China. E-mail: stone2009@126.com; hanyxt@163.com*

† Electronic supplementary information (ESI) available. See DOI: 10.1039/c8ra07396a

replaced by $S^{2-}$, $Se^{2-}$ and $MoO_4^{2-}$ to form the corresponding CoS,[37] CoSe,[38] and $CoMoO_4$ hollow cages.[39] Such MOF-assisted synthetic strategy provides more possibilities to obtain functional materials with improved physical and chemical properties.

Following the above considering, a new sheets-in-cage nanostructure composed by $Co_3O_4$ nanosheets inside and $NiCo_2O_4$ layer as outer shell has been designed and synthesized. The whole synthesis involves: (i) conversion reaction to produce ZIF-67@NiCo-LDH yolk@shell nanoparticles; (ii) hydrolysis reaction between ZIF-67@NiCo-LDH and hexamethylenetetramine (HMT) to form thin $Co(OH)_2$ nanosheets in the NiCo-LDH nanocage; (iii) annealing treatment in air atmosphere at 300 °C for 2 hours for the fabrication of final $Co_3O_4$@$NiCo_2O_4$ sheets-in-cage hollow nanoparticles. In our design, three important structural advantages should be pointed out. First, strongly coupled $NiCo_2O_4$ as outer shell is expected to bring higher electro-conductivity. Second, the inner hollow space could accommodate the large volume changes during the lithiation/delithiation process. Last, the encapsulated $Co_3O_4$ nanosheets may provide more active sits for lithium storage. As expected, in the following LIB application, the as-obtained $Co_3O_4$@$NiCo_2O_4$ sheets-in-cage nanoparticles exhibit enhanced LIB performance.

The ZIF-67 crystals are synthesized according to the previous report.[19] Scanning electron microscopy (SEM) transmission electron microscopy (TEM) and powder X-ray diffraction (XRD) are used as characterization methods. As shown in Fig. S1,† the product is uniform polyhedron with a particle size of ≈800 nm in average. The corresponding XRD pattern in Fig. S2† (black line) matches well with the previous reports,[19,37,38] indicating the product is in the pure phase of ZIF-67. Next, the above obtained ZIF-67 crystals are further reacted with $Ni(NO_3)_2$ in absolute ethanol. 40 min later, the products are collected and washed with ethanol for three times (details are shown in the ESI†).

With the data displayed in Fig. 1a–c, the as-obtained particles are uniform and monodisperse. Compared with the original ZIF-67 templates, they keep the dodecahedral morphology with the similar average particle size (≈800 nm). However, the outer surface becomes much rougher. Ultra-thin nanosheet as the building block can be clearly observed. A solid core can be found in each particle. And the clear gap is formed between the shell and solid core, indicating the formation of yolk@shell nanostructure. The corresponding XRD pattern is shown in Fig. S2† (red line). The specific diffraction peaks can be assigned to ZIF-67 crystal. By referring to the report,[40] it is considered $Co^{2+}$ is slowly dissolved from ZIF-67 in such synthesis, then oxidized to $Co^{3+}$ by $NO_3^-$. Further co-precipitation with $Ni^{2+}$ causes the formation of NiCo-LDH. Along with the hydrolysis reaction, $H^+$ is generated, and ZIF-67 is etched continuously. As a result, ZIF-67@NiCo-LDH yolk@shell nanostructure is obtained. Further prolonging the reaction time to three hours can cause the complete dissolution of the inner ZIF-67 core. As revealed by the TEM images in Fig. S3,† single-shelled NiCo-LDH nanocages are successfully produced.

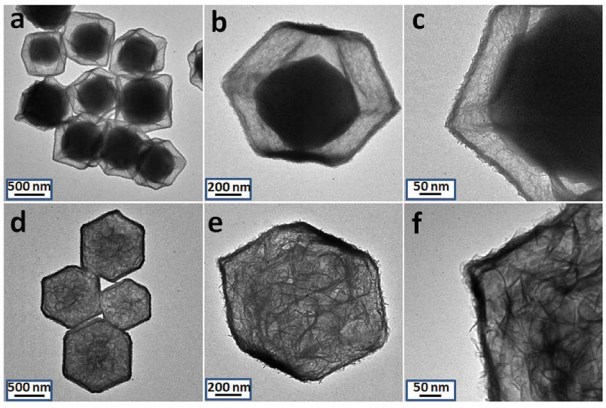


Fig. 1 TEM images of ZIF-67@NiCo-LDH yolk@shell nanoparticles (a to c) and $Co(OH)_2$@NiCo-LDH sheets-in-cage nanoparticles (d to f).

In next step, HMT is chosen as the weak alkali source. After heated at 90 °C for two hours, the color of the solution becomes from purple to yellow, indicating the complete conversion of inner ZIF-67 core. TEM images are first used to investigate the structure information. As shown in Fig. 1d–f, there is no obverse change in appearance. The overall structure is well maintained. The particles have the similar particle size, the outer surface is still rough and the thin nanosheets are clear to be observed. As expected, the inner solid cores are disappeared. Unexpected, large amount of thicker $Co(OH)_2$ sheets are formed and criss-cross in the nanocage. The formation mechanism could be understood as follow: $OH^-$ ions are first generated from HMT at high temperature, and then reacted with ZIF-67 to form the $Co(OH)_2$ nanosheets. The hollow space inside is large enough and the outer NiCo-LDH layer is stable to limit the expanded growth of $Co(OH)_2$ nanosheets, thus, the unique sheets-in-cage hybrid nanostructure is successfully synthesized. The XRD pattern of the as-obtained product is investigated and shown in Fig. S4.† The specific diffraction peaks of the solid ZIF-67 crystals disappeared completely, no clear diffraction peaks could be found, indicating the poor crystallization degree of the product.

Some control experiments are carried out to get a deeper understand about the formation mechanism. First, we tried to study the solvent-effect towards the structure evolution. Pure ethanol is used to replace the ethanol/water mixture. Two hours later, the colour of the solution is still purple, indicating the remain of ZIF-67. Fig. S5† displays the typical TEM images, that the change of the inner solid core is not obvious. Otherwise, there is no $Co(OH)_2$ nanosheets formed during the process. It reveals that water is necessary, which can participate in the decomposition of HMT to release $OH^-$ ions. Then, we increase the volume ratio of $H_2O$/ethanol to 2/1. With the TEM images shown in Fig. S6,† the sheets-in-cage hybrid nanostructure is also obtained. The similar phenomenon is also appeared when doubling the feeding amount of HMT (Fig. S7†). In such two conditions, large amount of $OH^-$ ions are generated, and the inner ZIF-67 cores can be dissolved completely. A control experiment is also done by using pure water as the solvent. In such condition, no precipitation is obtained. It is considered that $OH^-$ is generated fast, which causes the seriously damage of the three-dimensional cages. Thus, ultra-thin Co/Ni hydroxide nanosheets are well dispersed in water and hard to be collected by centrifugation. Next, we tried to use ZIF-67

 

crystals to instead of ZIF-67@NiCo-LDH yolk@shell nanoparticles to react with HMT directly. Four hours later, the original purple solution becomes to pink. The TEM images in Fig. S8† reveal that the as-obtained hollow particles show significant shrinkage with decreased size compared with the original ZIF-67 templates. No criss-crossed nanosheets formed inside the cages.

Such phenomenon indicates the outer NiCo-LDH layer is important for the formation of such sheets-in-cage nanostructure. The difference of crystal structure between NiCo-LDH and $Co(OH)_2$ prevents the expanded growth of $Co(OH)_2$ nanosheets. Otherwise, we also study the alkali effect. $NH_3H_2O$ is used to instead of HMT. The TEM images in Fig. S9† reveal that the inner hollow space cannot be maintained in such condition. Small black particles are formed and loaded on the surface of the nanosheets. However, when urea is used, similar sheets-in-cage hybrids are successful synthesized. Urea is much similar with HMT, they can provide $OH^-$ ions slowly, which is considered as the necessary condition for the formation of inner nanosheets.

Finally, the pre-synthesized sample is annealed in air at 300 °C for the formation of crystallized product. SEM, TEM, XRD and XPS have been used to characterize the structural and composition information. The typical SEM image is displayed in Fig. 2a and b. The particles can withstand the annealing treatment. Compared with the un-heated precursor, the polyhedron morphology has been maintained well with rough surface. The inner nanostructure is further investigated by TEM images. With the data shown in Fig. 2d–f, the hollow cage is filled with thin $Co_3O_4$ nanosheets. XRD pattern of the annealed products are taken and shown in Fig. 2c. Three diffraction peaks appear at $2\theta = 31.2°$, 36.8°, 44.8°, 59.4° and 65.3° which can be indexed to the (220), (311), (400), (511) and (400) planes of $Co_3O_4$. In addition, the composition of the product is further determined by EDX analysis. As shown in Fig. S10,† Co and Ni signals are clear observed. X-ray photoelectron spectroscopy (XPS) is further used to determine the chemical state of Co, Ni and O in $Co_3O_4/NiCo_2O_4$ sheets-in-cage sample. With the data shown in Fig. 3, there are two peaks appear at 779 eV and 795 eV, corresponding to the Co $2p_{3/2}$ and $2p_{1/2}$ spin orbit peaks, respectively. As shown in Fig. 3c, two strong peaks are observed at 854 and 872 eV, which could be assigned to the Ni $2p_{3/2}$ and $2p_{1/2}$ spin orbit, respectively. These results reveal that the presence of $Co^{2+}$, $Co^{3+}$ and $Ni^{2+}$ in the final product. Otherwise, the contents of Co and Ni are also calculated based on the XPS analysis, that the molar ratio of Co/Ni is ≈23/6. For better comparison, NiCo-LDH cages and ZIF-67 are also annealed in air under the same condition. With the typical TEM images shown in Fig. S11 and S12,† the single-shelled $NiCo_2O_4$ and $Co_3O_4$ nanocages are obtained.

Next, we further test the Li storage performance of the as-obtained $Co_3O_4$@$NiCo_2O_4$ sheets-in-cage nanoparticles. Fig. 4a displays the first four cyclic voltammogram (CV) curves of the $Co_3O_4$@$NiCo_2O_4$ electrode at a scan rate of 0.1 mV $s^{-1}$ in the potential window of 3 V to 0.01 V. There is a big difference between the first cycle and the others. It is clear two reduction peaks appeared at about 1.3 V and 0.8 V in the first discharge process, corresponding to the destruction and/or amorphization of their crystal structure and the reduction reaction between $Co_3O_4/NiCo_2O_4$ and Li, respectively.[41,42] During this process, irreversible solid electrolyte interface is also generated. For the first charge process, two wide peaks at 1.5 and 2.2 V are clearly observed, which could be attributed to the oxidation reaction between Co/Ni metal and $Li_xO$. Starting from the second cycle, there is an obverse shift of the main reduction peak from 0.8 to 1.0 V, which could be assign to the irreversible processes in first cycle. Importantly, the following CV curves overlap well, indicating the excellent reversibility and stability.

Fig. 4b is the charge–discharge voltage profiles of the $Co_3O_4$@$NiCo_2O_4$ sheets-in-cage nanocages at a current density of 100 mA $g^{-1}$ for 1st and 2nd cycle. In the first cycle, the discharge voltage plateaus related the reduction reaction of $Co_3O_4/NiCo_2O_4$ and the charge voltage about the corresponding oxidation reaction appears at 1.2 and 2.1 V, respectively. Starting from the second cycle, the discharge voltage plateau is shifted, indicating the changes of the structure during the

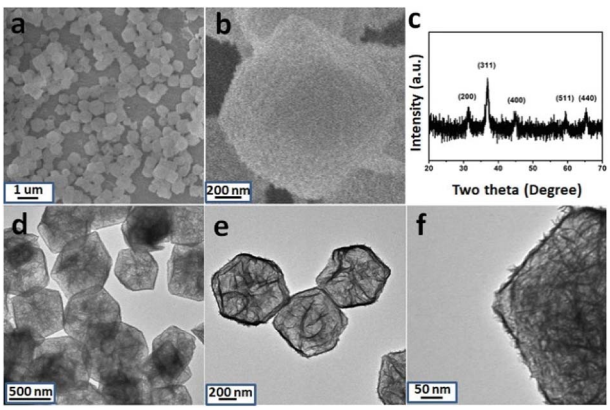


Fig. 2 SEM (a and b), TEM images (d to f) and XRD pattern (c) of $Co_3O_4$@$NiCo_2O_4$ sheets-in-cage hybrid nanoparticle.

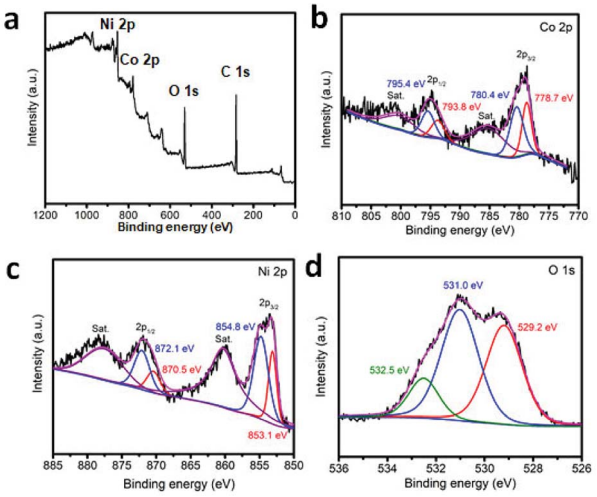


Fig. 3 XPS spectra of $Co_3O_4$@$NiCo_2O_4$ sheets-in-cage hybrid nanoparticles.

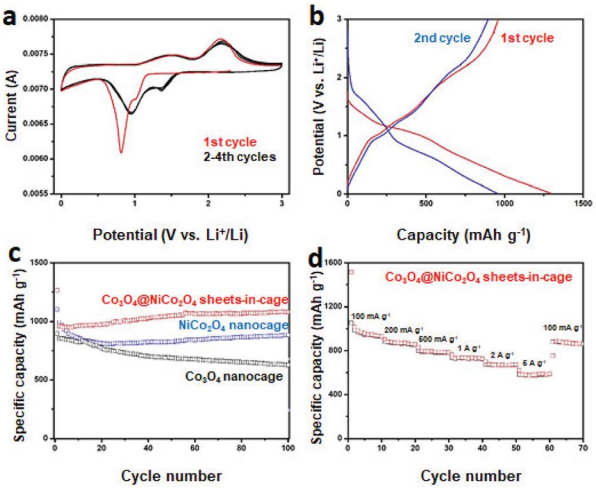


Fig. 4 Cyclic voltammogram measurements at a scan rate of 0.1 mV $s^{-1}$ (a), charge–discharge voltage profiles in the first and second cycles at a current density of 100 mA $g^{-1}$ (b) and rate performance at various current densities (d) of the $Co_3O_4$@$NiCo_2O_4$ sheets-in-cage electrodes; cycling performances (c) of $Co_3O_4$@$NiCo_2O_4$, $NiCo_2O_4$ and $Co_3O_4$ nanocages at a current density of 100 mA $g^{-1}$ for 100 successfully cycles (discharged capacity).

charging and discharging process. These results match well with the CV measurements.

Fig. 4c shows the cycling performance of $Co_3O_4$@$NiCo_2O_4$ sheets-in-cage nanocages in the current density of 100 mA $g^{-1}$. In the first discharge process, an ultra-high capacity of 1262 mA h $g^{-1}$ with a coulombic efficiency of 62% is achieved. After then, the second cycle delivers a capacity of 959 mA h $g^{-1}$. The capacity is slightly decreased in the following ten cycles, and then increased to 1083 mA h $g^{-1}$ after 100 cycles. The increase of the capacities could be attributed to the activation effect. The electrode material can become more and more accessible to host lithium ions during the charge/discharge process.[43–45] Furthermore, each cycle exhibits a high coulombic efficiency of around 99% excepted the first cycle. For comparison, single-shelled $NiCo_2O_4$ and $Co_3O_4$ nanocages are also used as anode materials for LIBs. As shown in Fig. 4c blue line, $NiCo_2O_4$ nanocage delivers a specific capacity of 882 mA h $g^{-1}$ after 100 cycles at a current density of 100 mA $g^{-1}$. And the capacity of $Co_3O_4$ nanocage fads fast, a capacity of only 626 mA h $g^{-1}$ is obtained after 100 cycles (Fig. 4c black line). In addition, the long-term cycling performance of $Co_3O_4$@$NiCo_2O_4$ sheets-in-cage nanocage at higher current density of 1 A $g^{-1}$ is also tested. With the data displayed in Fig. S13,† a high capacity of 658 mA h $g^{-1}$ is remained after 200 successful cycles. We also collect the $Co_3O_4$@$NiCo_2O_4$ sheets-in-cage samples after 30 cycles at the current density of 100 mA $g^{-1}$. The corresponding TEM images are shown in Fig. S14.† Although the shrink of the nanostructure is observed, the overall sheets-in-cage hollow nanostructure is maintained well, indicating the high structural stability.

The rate performance is another important factor for anode materials. Fig. 4d shows the rate performance of the as-obtained $Co_3O_4$@$NiCo_2O_4$ sheets-in-cage nanocage by gradually increasing the current density from 0.1 to 5 A $g^{-1}$ and then returning it to 0.1 A $g^{-1}$. It delivers specific capacities of 942, 872, 786, 734, 668, and 578 mA h $g^{-1}$ at the current densities of 0.1, 0.2, 0.5, 1, 2 and 5 A $g^{-1}$, respectively. Impressively, when the current density returned to 100 mA $g^{-1}$, the capacity is fast increased to 890 mA h $g^{-1}$, indicating the excellent rate performance and structural stability. For comparison, the average discharge capacities of the as-obtained $NiCo_2O_4$ and $Co_3O_4$ nanocages are measured to be 926, 845, 760, 705, 642, 550, and 735, 587, 542, 503, 475, 311 mA h $g^{-1}$ at a current density of 0.1, 0.2, 0.5, 1, 2 and 5 A $g^{-1}$ respectively, which is much lower than the $Co_3O_4$@$NiCo_2O_4$ sheets-in-cage material (with the data shown in Fig. S15†).

Electrochemical impedance spectroscopy (EIS) is adopted to further investigate the electrochemical kinetics difference among the as-obtained three samples. With the data shown in Fig. S16,† the Nyquist plots are consisted of a semicircle at the high to medium frequencies followed by a sloped line at the low frequencies. It is obvious that $Co_3O_4$@$NiCo_2O_4$ sheets-in-cage electrode has the lowest charge transfer resistance, which could be a big benefit to the LIB performance.

Such enhanced LIB property of the $Co_3O_4$@$NiCo_2O_4$ sheets-in-cage nanocages could be attributed to the following features. First, the inner thin $Co_3O_4$ nanosheets have larger surface area, which can provide massive active sites for lithium storage. Second, the formation of hollow space in $NiCo_2O_4$ nanocages is considered as the efficient way to alleviate the volume change and buffer the induced strain during quick charge/discharge process. Thirdly, the outer surface is strongly coupled $NiCo_2O_4$ mixed metal oxide, which is expected to bring higher electro-conductivity compared with the $Co_3O_4$ component.

## Conclusions

In summary, a facile synthesis has been developed for the fabrication of $Co_3O_4$@$NiCo_2O_4$ sheets-in-cage nanostructures. Uniform ZIF-67 crystals are chosen as the starting hard templates, following by an ion-exchange reaction to produce ZIF-67@NiCo-LDH yolk@shell nanoparticles, and subsequent hydrolyzation reaction with HMT realize the conversion of inner ZIF-67 cores to $Co(OH)_2$ thin nanosheets. An annealing process is finally applied under air atmosphere at 300 °C for the final formation of $Co_3O_4$@$NiCo_2O_4$ sheets-in-cage nanostructures. In the following LIB test, the as-prepared $Co_3O_4$@$NiCo_2O_4$ sheets-in-cage nanoparticles exhibit excellent performance for Lithium storage, not only the high specific capacity after long-term cycling, but also the excellent rate performance. Such structural design and wet-chemistry synthetic strategy may hold great promise for the fabrication of functional nanomaterials with enhanced properties for energy storage and conversion.

## Conflicts of interest

There are no conflicts to declare.

## Acknowledgements

This work was supported by National Natural Science Foundation of China (No. 51672103) and Natural Science Foundation of Jilin Province (No. 20160204069GX, No. JJKH20170236KJ and JJKH20170243KJ).

## Notes and references

1 B. Dunn, H. Kamath and J.-M. Tarascon, *Science*, 2011, **334**, 928–935.
2 J. W. Choi and D. Aurbach, *Nat. Rev. Mater.*, 2016, **1**, 16013.
3 P. Simon, Y. Gogotsi, P. Simon and Y. Gogotsi, *Nat. Mater.*, 2008, **7**, 845–854.
4 Y. Yang, G. Zheng, S. Misra, J. Nelson, M. Toney and Y. Cui, *J. Am. Chem. Soc.*, 2012, **134**, 15387–15394.
5 Y. Wang, J. Wu, Y. Tang, X. Lü, C. Yang, M. Qin, F. Huang, X. Li and X. Zhang, *ACS Appl. Mater. Interfaces*, 2012, **4**, 4246–4250.
6 F. Wang, X. Wu, C. Li, Y. Zhu, L. Fu, Y. Wu and X. Liu, *Energy Environ. Sci.*, 2016, **9**, 3570–3611.
7 F. Hu and T. Song, *RSC Adv.*, 2017, **7**, 54203–54212.
8 Z. Gong and Y. Yang, *Energy Environ. Sci.*, 2011, **4**, 3223–3242.
9 M. Aslam, S. Shah, S. Li and C. Chen, *J. Mater. Chem. A*, 2018, **6**, 14083–14090.
10 C. Zhang, B. Lu, F. Cao, Z. Yu, H. Cong and S. Yu, *J. Mater. Chem. A*, 2018, **6**, 1428–1436.
11 C. Yan, G. Chen, X. Zhou, J. Sun and C. Lv, *Angew. Chem., Int. Ed.*, 2016, **26**, 7060–7064.
12 D. Gu, W. Li, F. Wang, H. Bongard, B. Spliethoff, W. Schmidt, C. Weidenthaler, Y. Xia, D. Zhao and F. Schüth, *Angew. Chem., Int. Ed.*, 2015, **54**, 7060–7064.
13 B. Wang, X. Lu and Y. Tang, *J. Mater. Chem. A*, 2015, **3**, 9689–9699.
14 B. Guan, X. Yu, H. Wu and X. Lou, *Adv. Mater.*, 2017, **29**, 1703614.
15 R. Wu, X. Qian, K. Zhou, J. Wei, J. Lou and P. Ajayan, *ACS Nano*, 2014, **8**, 6297–6303.
16 J. Qi, X. Lai, J. Wang, H. Tang, H. Ren, Y. Yang, Q. Jin, L. Zhang, R. Yu, G. Ma, Z. Su, H. Zhao and D. Wang, *Chem. Soc. Rev.*, 2015, **44**, 6749–6773.
17 J. Zhang, H. Ren, J. Wang, J. Qi, R. Yu, D. Wang and Y. Liu, *J. Mater. Chem. A*, 2016, **4**, 17673–17677.
18 J. Wang, N. Yang, H. Tang, Z. Dong, Q. Jin, M. Yang, D. Kisailus, H. Zhao, Z. Tang and D. Wang, *Angew. Chem., Int. Ed.*, 2013, **52**, 6417–6420.
19 H. Hu, B. Guan, B. Xia and X. Lou, *J. Am. Chem. Soc.*, 2015, **137**, 5590–5595.
20 X. Wang, L. Yu, B. Guan, S. Song and X. Lou, *Adv. Mater.*, 2017, **29**, 1801211.
21 Y. Lu, J. Nai and X. Lou, *Angew. Chem., Int. Ed.*, 2018, **57**, 2899–2903.
22 B. Guan, A. Kushima, L. Yu, S. Li, J. Li and X. Lou, *Adv. Mater.*, 2018, **30**, 1605902.
23 S. Parka, J. Kima, J. Kimb and Y. Kang, *Mater. Charact.*, 2017, **132**, 320–329.
24 J. Zhao, Y. Zou, X. Zou, T. Bai, Y. Liu, R. Gao, D. Wang and G. Li, *Nanoscale*, 2014, **6**, 7255–7262.
25 X. Yang, J. Chen, Y. Chen, Pi. Feng, H. Lai, J. Li and X. Luo, *Nano-Micro Lett.*, 2017, **10**, 15.
26 X. Yu and X. Lou, *Adv. Energy Mater.*, 2018, **8**, 1701592.
27 J. Guo, Z. Yin, X. Zang, Z. Dai, Y. Zhang, W. Huang and X. Dong, *Nano Res.*, 2017, **10**, 405–414.
28 X. Qi, W. Zheng, G. He, T. Tian, N. Du and L. Wang, *Chem. Eng. J.*, 2017, **309**, 426–434.
29 S. Park, S. Yang and Y. Kan, *Chem. Eng. J.*, 2018, **349**, 214–222.
30 J. Cheng, Y. Lu, K. Qiu, H. Yan, J. Xu, L. Han, X. Liu, J. Luo, J. Kim and Y. Luo, *Sci. Rep.*, 2015, **5**, 12099.
31 B. Liu, J. Zhang, X. Wang, G. Chen, D. Chen, C. Zhou and G. Shen, *Nano Lett.*, 2012, **12**, 3005–3011.
32 W. Huang, S. Li, X. Cao, C. Hou, Z. Zhang, J. Feng, L. Ci, P. Si and Q. Chi, *ACS Sustainable Chem. Eng.*, 2017, **5**, 5039–5048.
33 X. Xu, R. Cao, S. Jeong and J. Cho, *Nano Lett.*, 2012, **12**, 4988–4991.
34 D. Sun, L. Ye, F. Sun, H. García and Z. Li, *Inorg. Chem.*, 2017, **56**, 5203–5209.
35 S. Hou, X. Xu, M. Wang, Y. Xu, T. Lu, Y. Yao and L. Pan, *J. Mater. Chem. A*, 2017, **5**, 19054–19061.
36 T. Wang, Q. Zhou, X. Wang, J. Zheng and X. Li, *J. Mater. Chem. A*, 2015, **3**, 16435–16439.
37 P. Zeng, J. Li, M. Ye, K. Zhuo and Z. Fang, *Chem.–Eur. J.*, 2017, **23**, 9517–9524.
38 S. Park, J. Park and Y. Kang, *ACS Appl. Mater. Interfaces*, 2018, **10**, 16531–16540.
39 Y. Li, H. Xu, H. Huang, C. Wang, L. Gao and T. Ma, *Chem. Commun.*, 2018, **54**, 2739–2742.
40 Z. Jiang, Z. Li, Z. Qin, H. Sun, X. Jiao and D. R. Chen, *Nanoscale*, 2013, **5**, 11770–11775.
41 Y. H. Li, X. W. Wu, S. L. Wang, W. Q. Wang, Y. H. Xiang, C. H. Dai, Z. X. Liu, Z. Q. He and X. m. Wu, *RSC Adv.*, 2017, **7**, 36909–36916.
42 L. L. Li, Y. L. Cheah, Y. Ko, P. Teh, G. Wee, C. L. Wong, S. J. Peng and M. Srinivasan, *J. Mater. Chem. A*, 2013, **1**, 10935–10941.
43 J. Jamnik and J. Maier, *Phys. Chem. Chem. Phys.*, 2003, **5**, 5215–5220.
44 J. F. Chen, Q. Ru, Y. D. Mo, S. J. Hu and X. H. Hou, *Phys. Chem. Chem. Phys.*, 2016, **18**, 18949–18957.
45 F. X. Wang, C. Wang, Y. J. Zhao, Z. C. Liu, Z. Chang, L. J. Fu, Y. S. Zhu, Y. P. Wu and D. Y. Zhao, *Small*, 2016, **12**, 853–859.